FEBRUARY 06 2023

The broadband transport theory approach to model internal wave induced scattering across deep water acoustic time-fronts

Sivaselvi Periyasamy; Tarun K. Chandrayadula

J Acoust Soc Am 153, 895–908 (2023)
https://doi.org/10.1121/10.0017102

JASA ARTICLE

The broadband transport theory approach to model internal wave induced scattering across deep water acoustic time-fronts

Sivaselvi Periyasamy and Tarun K. Chandrayadula[a)]
Department of Ocean Engineering, Indian Institute of Technology Madras, Chennai, Tamil Nadu, India

ABSTRACT:
There are currently no models to fully predict the effects of internal wave induced scattering on acoustic pulses. Existing models, which predict time domain statistics, either use the ray-based path integral method or Monte Carlo type simulations. The path integral method fails to accurately predict all of the effects of scattering. The Monte Carlo methods base the statistics on ensemble averages and are not physics-based models. This paper overcomes these limitations by using the modes of the waveguide in a transport theory application. The transport theory equations have, thus far, been used only to explain diffusion of mode intensities and decorrelation due to internal waves at individual frequencies. This paper extends the current narrowband application predict mode correlations across different frequencies and, from that, the broadband time-front, time wander, travel time bias, and the amount of spread in intensity across time and depth. To validate these predictions, this paper uses separate parabolic equation simulations. The comparisons between the two are good, suggesting a success for the mode-based transport theory approach. https://doi.org/10.1121/10.0017102

(Received 13 July 2022; revised 21 December 2022; accepted 12 January 2023; published online 6 February 2023)

[Editor: Oleg A. Godin] Pages: 895–908

I. INTRODUCTION

A typical model for a deep water acoustic time-front consists of well-defined ray-like early arrivals and an energetic finale with a complicated interference pattern (Munk *et al.*, 1995). Internal wave induced sound speed perturbations cause scattering of the time-front. The scattering effects include loss or gain in intensity level, temporal spreading, travel time fluctuations or wander, and travel time bias. In spite of the scattering, the early ray-like arrivals are still coherent across depth. The finale, however, does not hold its interference pattern and is much smeared in time and depth. The time-front also shows energy at depths where no signals are expected to arrive. The areas, called "shadow zones," are, thus, ensonified due to scattering (Dushaw *et al.*, 1999; Van Uffelen *et al.*, 2009).

Previous studies on pulse propagation through internal waves used ray-based path integral methods to predict the travel time statistics, such as pulse wander and temporal spread (Andrew *et al.*, 2016; Colosi *et al.*, 2019; Colosi *et al.*, 1999; Reynolds *et al.*, 1985). Ray methods, by definition, are ideally suited for infinitely high frequencies. The rays, hence, do not account for the diffraction effects in the finale. The path integral method, in its current form, does not adequately model the temporal spread of the finale (Andrew *et al.*, 2016). Further, the path integral method relies on calculations around eigenrays predicted for the background environment. In the shadow zones, eigenray calculations, which do not include scattering, predict nil arrivals. The path integral method, thus, cannot predict the signal statistics in those areas. In addition to ray methods, parabolic equation (PE) simulations have also been used to predict the pulse statistics (Colosi *et al.*, 1994; Udovydchenkov *et al.*, 2012; Van Uffelen *et al.*, 2009; Van Uffelen *et al.*, 2010). The PE statistics are estimated from Monte Carlo runs for a specific set of internal wave model parameters. It is, though, difficult to relate the physics and statistics in a Monte Carlo application.

To include all the relevant propagation physics, this paper uses the modes of deep water waveguide. The modes, $\phi_n(z)$, are solutions of the depth dependent wave equation,

$$\frac{d^2\phi_n(z)}{dz^2} + \left(\omega^2/c^2(z) - k_n^2\right)\phi_n(z) = 0. \tag{1}$$

The mode shapes are a function of frequency, ω, and the sound speed profile, $c(z)$. In the real ocean, the sound speed varies as a function of range, r, and, hence, the mode shapes, $\phi_n(z)$, as well. The significant changes in the sound speed across range are due to large-scale oceanographic variability. This paper, however, assumes a constant background across the range and, hence, uses the same set of modes for all of the calculations. The pressure field, $p(r,z,\omega)$, at range r, depth z, and frequency ω, can be expressed as

$$p(r,z,\omega) = \sum_{n=1}^{N} \frac{a_n(r,\omega)\phi_n(z,\omega)e^{ik_n r}}{\sqrt{k_n r}}, \tag{2}$$

where $a_n(r,\omega)$ are complex mode amplitudes, and k_n the respective wavenumbers. The initial mode amplitudes are given by $a_n(r,\omega) = \phi_n(z_s,\omega)$, where z_s is the source depth. On further propagation in range, the modes suffer

[a)]Electronic mail: tkchandr@iitm.ac.in

cylindrical spreading, $1/\sqrt{k_n r}$, and incur phases equal to k_{nr} to travel with group velocities,

$$v_{g,n} = \frac{d\omega}{dk_n}. \tag{3}$$

To connect the mean intensity, $\langle I(r,z,t)\rangle$, and the mode amplitudes, this paper express the time-front as a Fourier integral, where

$$\langle I(r,z,t)\rangle = \int_{\omega_1}\int_{\omega_2} \langle p(r,z,\omega_1)p^*(r,z,\omega_2)\rangle e^{i(\omega_1-\omega_2)t} d\omega_1 d\omega_2, \tag{4}$$

and $\langle p(r,z,\omega_1)p^*(r,z,\omega_2)\rangle$ is the cross-frequency correlation function of the pressure field. Using Eq. (2), the expression for mean intensity becomes

$$\langle I(r,z,t)\rangle = \int_{\omega_1}\int_{\omega_2} \sum_{n=1}^{N}\sum_{p=1}^{N} \frac{\langle a_n(\omega_1)a_p^*(\omega_2)\rangle(r)}{r} \times \frac{\phi_n(z,\omega_1)\phi_p(z,\omega_2)}{\sqrt{k_n(\omega_1)k_p(\omega_2)}} e^{i(\omega_1-\omega_2)t} d\omega_1 d\omega_2, \tag{5}$$

where $\langle a_n(\omega_1)a_p^*(\omega_2)\rangle(r)$ denotes the frequency correlation of modes (broadband mode statistics) across range. The cross-mode cross-frequency correlations are the central focus of this paper. Virovlyansky (2015) and Virovlyansky and Kazarova (2016) used the Wentzel-Kramers-Brillouin (WKB) approximation to derive a ray-based approximation to modes and their correlation functions across range. The WKB methods are attractive because they yield analytical expressions for the cross-mode correlations and, yet, ideally are suited only for high frequencies. Also, Virovlyansky (2015) and, later, Virovlyansky and Kazarova (2016) only presented simulations for limited ranges with discrepancies in the model comparisons for the longest ranges around 500 km. The WKB methods are also better suited for the early arrivals, which are more akin to rays than the signals around the finale. This paper will predict scattering statistics for long ranges by going up to 1000 km and focusing on all parts of the time-front and, hence, eschews any WKB approximations and uses the exact modes of the waveguide as computed from Eq. (1).

Transport theory is used here to predict the cross-frequency correlation of the modes across range. The transport theory methods are basically diffusion equations, which are mathematically similar to approaches in heat and semiconductor physics (Van Kampen, 2007). In underwater acoustics, transport theory has been applied to model the diffusion of second moments of mode amplitudes, $\langle a_n(\omega)a_p^*(\omega)\rangle$, across range (Colosi *et al.*, 2013; Colosi and Morozov, 2009; Creamer, 1996). Transport theory connects the rate of spread of energy among the acoustic modes with oceanographic parameters such as strength of the internal waves and the correlation-scales of the Garrett-Munk (GM) wave spectrum (Garrett and Munk, 1972, 1975). For a broadband application, Chandrayadula *et al.* (2013a) used the adiabatic phase approximation to construct the pulses for the lowest modes and compared them with observations from the Philippine Sea 2010 (PhilSea10) experiment. The adiabatic approximation was sufficient to model the lowest modes (1–15) in the PhilSea10 experiment. Chandrayadula *et al.* (2013a) used the mode travel time sensitivity kernels to suggest that the reason for such good agreement with only an approximate model was potentially because of the nature of the dispersion for the lowest modes in the background PhilSea10 acoustic environment (Worcester *et al.*, 2013). For the time-front predictions of the finale in PhilSea10, which involves combinations across the low modes, however, Periyasamy *et al.* (2022) showed that the adiabatic approximation was insufficient and required solving the transport theory for all the cross-modal cross-frequency correlations. It is currently not known if the adiabatic approximation is applicable to the low modes in a universal manner without regard to the background environment. Also, the calculations for the finale by Periyasamy *et al.* (2022) only used a subset of modes, which is not enough to model the other parts of the time-front. A full test of the broadband transport theory, which includes all of the parts of the time-front is awaited. Some of the scattering effects, such as the stability of the early ray-like arrivals, and the ensonification of shadow zones, which involve the high modes, have still not been examined fully.

This paper performs broadband transport theory predictions to model the mean time-front for a source bandwidth of 60–90 Hz up to 1000 km. There are two reasons to prefer this bandwidth. The first reason is that these low frequencies keep the modes at a manageable number in the transport theory calculations. The second is that the frequencies are similar to prior deep water experiments in the North Pacific Ocean (Colosi and the ATOC Group, 1999; Mercer *et al.*, 2009). The predictions, thus, use the background environmental profiles (sound speed, buoyancy profile, potential sound speed gradient, and the root mean square (RMS) sound speed perturbations) based on *in situ* measurements during the Long Range Ocean Acoustic Propagation Experiment (LOAPEX) conducted in 2004, which was a part of the larger North Pacific Acoustic Laboratory exercise (Fig. 1). Comparison of the predictions to observations from an actual long range experiment would entail including realistic effects such as variation of the background sound speed profile across range. The transport theory model in its current form only assumes a constant background profile and is not equipped to handle variations across range. Also, the low frequency experiments in the North Pacific did not contain observations using a full water-column spanning array, which will be compared herein. To test the model, this paper, thus, resorts to PE simulations that use the background SSP in Fig. 1. Multiple realizations of the internal wave effects based on the buoyancy and adiabatic sound speed gradient profiles in Fig. 1 were generated using the method suggested by Colosi and Brown (1998) and added to the background SSP. Figure 1 shows the RMS value of the sound speed perturbations added to the constant

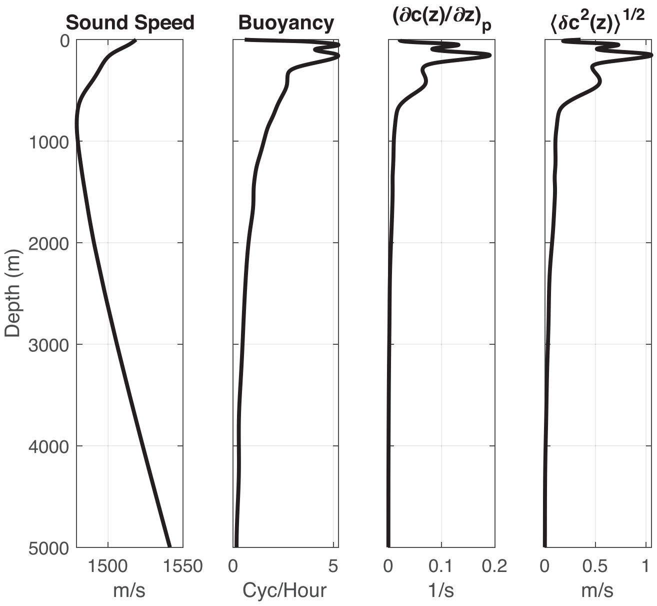

FIG. 1. The mean sound speed profile, buoyancy frequency profile, potential sound speed gradient ($(\partial c(z)/\partial z)_p$), and RMS of the sound speed variations, ($\langle \delta c^2(z)\rangle^{1/2}$).

background. There were a total of 100 such PE simulations. The mean intensity and various time-front statistics predictions from the model are then compared with averages from the PE simulations.

The remaining sections of this paper are organized as follows. Section II sets up the transport theory for broadband mode statistics predictions and discusses the details of the PE simulations. There are also complementary simulations based on the adiabatic model. There are two reasons for including the adiabatic model. The first is that the adiabatic model includes mostly just the time wander induced by internal waves and not the effects of interference that occur due to cross-frequency decorrelation. This paper will test if such a model is sufficient for all of the modes in the North Pacific environment. The second is that the adiabatic model provides analytical predictions for cross-modal decorrelations, which are later used to predict the fluctuation in arrival times for the modes, and the time-front. Next, Sec. III compares the transport theory predictions with statistics estimated from PE simulations. Finally, Sec. IV discusses the results and concludes the paper.

II. TRANSPORT THEORY PREDICTIONS AND PE SIMULATIONS

Prior to the transport theory equations, it is useful to briefly review the background of mode propagation through internal waves. In a range-independent environment where the sound speed is constant across range, the mode amplitudes propagate independently and the phases given by the predictions from the background profile. However, in an environment where the sound speed varies from one range to the other, the coupled mode theory predicts that the mode amplitudes interfere with each other, and the individual phases are perturbed from their background values. For an environment containing diffuse internal waves, such as described by the GM model, where the SSP is continuously perturbed across different range scales, the coupled mode theory equations can be modeled as stochastic differential equations. Dozier and Tappert (1978a,b) produced the seminal work in this field to show that internal wave induced coupling causes mode intensities to diffuse across mode number. This coupling continues to infinitely long ranges until equipartition in mode intensities and Rayleigh statistics for scintillation. Dozier and Tappert (1978a,b), though, neglected cross-modal correlations in their predictions for intensities. Later, Colosi and Morozov (2009) and Colosi *et al.* (2013) explicitly predicted the cross-modal correlations. Chandrayadula *et al.* (2013a) then verified the predictions against observations. For broadband mode statistics, such as scattering in mode pulses or the time-front, there have been many experimental observations and simulations (Chandrayadula *et al.*, 2013b; Colosi and Flatte, 1996; Wage *et al.*, 2003; Udovydchenkov and Brown, 2008; Udovydchenkov *et al.*, 2012; Wage *et al.*, 2005). The observations from experiments and simulations suggest that modes initially propagate as independent pulses with only a time wander due to the variation in the average sound speed and, at further ranges, show multiple arrivals. The scattering effects were more obvious in the finale, where the arrival structure seemed to be diffuse in time and depth. However, there have been no analytical models to fully predict the mode arrival structure in broadband, which requires the cross-mode cross-frequency correlations [Eq. (5)].

The transport theory equations for the cross-frequency cross-mode correlations are given by Colosi (2016),

$$\begin{aligned}\frac{d\langle a_n(\omega_1)a_p^*(\omega_2)\rangle(r)}{dr} &= i(k_{n1}-k_{p2}^*)\langle a_n(\omega_1)a_p^*(\omega_2)\rangle \\ &\quad -\sum_{m=1}^{N}\sum_{q=1}^{N}\langle a_m(\omega_1)a_q^*(\omega_2)\rangle I_{mn1,qp2}^* \\ &\quad +\langle a_q(\omega_1)a_m^*(\omega_2)\rangle I_{mp2,qn1}^* \\ &\quad -\langle a_n(\omega_1)a_q^*(\omega_2)\rangle I_{mp2,qm2}^* + \langle a_n(\omega_1)a_q^*(\omega_2)\rangle I_{mn1,qm1}^*,\end{aligned} \tag{6}$$

where k_{n1} and k_{p2} are the wavenumbers for modes, n and p, at frequencies, ω_1 and ω_2, respectively. The expression for the scattering matrix,

$$I_{mn1,qp2} = \sum_{j=1}^{J} H(j)G_{mn1}(j)G_{qp2}(j)\int_0^\infty dk_h F_1(k_h) \times \begin{cases} \dfrac{1}{\sqrt{k_h^2-k_{pq2}^2}}, & 0 \le |k_{pq2}| < k_h, \\ \dfrac{i\,\mathrm{sign}(k_{pq2})}{\sqrt{k_{pq2}^2-k_h^2}}, & 0 \le k_h < |k_{pq2}|, \end{cases} \tag{7}$$

is a weighted summation of coupling matrices across the internal wave mode number, j. The coupling matrices, $G_{mn1}(j)$, are given by

$$G_{mn1}(j) = \frac{\zeta_0 k_{01}^2}{c_0}\sqrt{\frac{2}{k_{n1}k_{m1}}}\int_0^D dz\left(\frac{\partial c(z)}{\partial z}\right)_p \times \left(\frac{N_0}{N(z)}\right)^{1/2}\sin\left[\pi j\hat{z}(z)\right]\frac{\phi_{n1}(z)\phi_{m1}(z)}{\rho_0(z)}. \quad (8)$$

For calculating G_{mn1} in Eq. (8), ζ_0 is a reference internal wave displacement, $k_{01} = \omega_1/c_0$ is a reference acoustic wavenumber, $(\partial c(z)/\partial z)_p$ is the potential sound speed gradient, N_0 is a reference buoyancy frequency, $N(z)$ is the buoyancy frequency profile, $\hat{z}(z)$ is the Wentzel-Kramers-Brillouin-Jeffreys (WKBJ) stretched vertical coordinate, and $k_{pq} = k_p - k_q$ is the difference modal wavenumber. A similar expression holds for $G_{qp2}(j)$ using modes at frequency ω_2. The expressions for GM vertical mode number spectrum, $H(j)$, and internal wave spectrum, $F_1(k_h)$, are given by

$$H(j) = \frac{1}{M_j}\frac{1}{j + j_*}, \quad (9)$$

$$F_1(k_h) = \frac{4}{\pi}\frac{k_h^2\hat{k}_j}{(k_h^2 + \hat{k}_j^2)^2}. \quad (10)$$

The parameter, j_*, called the "modal bandwidth," $M_j = \sum_{j=i}^{J_{\max}} 1/(j^2 + j_*^2)$ is the normalization constant for $J_{\max}$ number of internal wave modes; k_h the internal wave horizontal wavenumber; $\hat{k}_j = \pi j f / N_0 B$ is the internal wave wavenumber, which depends on the Coriolis frequency, f; $N_0 B = \int_0^D N(z)dz$, where $N(z)$ is the buoyancy frequency profile and D the total water depth.

The complementary simulations using the adiabatic version only include the travel time wander due to perturbation in sound speed across range and not all the effects of cross-frequency decorrelation (Chandrayadula *et al.*, 2020). Although the wander is constant across the bandwidth, the individual frequency components are slightly decorrelated with each other due to the different phases they incur. This approach performs separate predictions for each frequency (Colosi and Morozov, 2009) and approximates the cross-frequency coherences by using the adiabatic phase structure-function. The cross-mode cross-frequency correlations in the adiabatic approximation are given by

$$\begin{aligned}\langle a_n(\omega_1)a_p^*(\omega_2)\rangle(r) &= \sqrt{\langle|a_n(r,\omega_1)|^2\rangle\langle|a_p(r,\omega_2)|^2\rangle} \\ &\times \mathrm{sign}(a_n(0,\omega_1))\mathrm{sign}(a_p(0,\omega_2)) \\ &\times e^{i(k_n(\omega_1)-k_p(\omega_2))r}e^{-(I_{nn,nn}(\omega_1)+I_{pp,pp}(\omega_2)-2I_{nn,pp}(\omega_1,\omega_2))r}, \quad (11)\end{aligned}$$

where $I_{nn,nn}(\omega_1)$ and $I_{pp,pp}(\omega_2)$ are the scattering matrices from Eq. (7), calculated for mode n at angular frequency ω_1 and mode p at ω_2, respectively. The quantities $\langle|a_n(r,\omega_1)|^2\rangle$ and $\langle|a_p(r,\omega_2)|^2\rangle$ are mode energies at ω_1 and ω_2, respectively. The expression for the mean travel time variance at the center frequency, $\omega_c = (\omega_1 + \omega_2)/2$, and $\Delta\omega = \omega_2 - \omega_1$ is

$$\begin{aligned}\langle\tau_n^2\rangle = \frac{2}{\Delta\omega^2}(&I_{nn,nn}(\omega_c+\Delta\omega/2)+I_{nn,nn}(\omega_c-\Delta\omega/2) \\ &-2I_{nn,nn}(\omega_c+\Delta\omega/2,\omega_c-\Delta\omega/2))r. \quad (12)\end{aligned}$$

The "travel time wander" is the RMS of the fluctuations, $\sqrt{\langle\tau_n^2\rangle}$.

Both Eqs. (6) and (11), for the full transport theory and the adiabatic theory, respectively, are used for modes 1–75 to predict the cross-mode cross-frequency coherence,

$$\overline{\langle a_n(\omega_1)a_p^*(\omega_2)\rangle(r)} = \frac{\langle a_n(\omega_1)a_p^*(\omega_2)\rangle(r)}{\sqrt{\langle|a_n(\omega_1)(r)|^2\rangle\langle|a_p(\omega_2)(r)|^2\rangle}}, \quad (13)$$

the mean intensity of the mode pulse,

$$\langle|\alpha_n(r,t)|^2\rangle = \int_{\omega_1}\int_{\omega_2}\langle a_n(\omega_1)a_n^*(\omega_2)\rangle(r)e^{i(\omega_1-\omega_2)t}\,d\omega_1\,d\omega_2, \quad (14)$$

the time-front, $\langle I(r,z,t)\rangle$, based on Eq. (5), and the RMS wander from Eq. (12). This paper also estimates the temporal "spread," which describes the total width of the pulse. In the absence of internal wave scattering, the background pulse width is approximately the sum of only (1/source bandwidth), and the dispersion induced spread for the source frequencies, which differs from one mode to the other. When internal wave perturbations cause scattering, there are two more additions to the spread. The first is the RMS wander of the pulse, which stretches the average pulse in time. The second is the coupling-induced multipath, which also smears the mean intensity temporally. There are no analytical expressions for the coupling-induced temporal-spread. In the absence of such analytical expressions, this paper, thus, uses the average intensities [Eq. (14)] and, from that, estimates the temporal width.

Table I lists the parameters used in the transport theory calculations. For the internal wave simulations, this paper used the same parameters that were previously used by Chandrayadula *et al.* (2013a). Colosi (2015) suggests increasing the number of internal wave modes, $J_{\max}$, to 900 from the previous number of 50 to account for shear

TABLE I. Simulation parameters for transport theory predictions.

Reference sound speed (c_0)	1480 m/s
Source depth (z_s)	800 m
Frequency resolution	0.33 Hz
Latitude	30°
Reference buoyancy frequency (N_0)	3 cycles/h
Number of internal wave modes ($J_{\max}$)	50
Reference internal wave displacement (ζ_0)	7.3 m
Modal bandwidth (j_*)	3

https://doi.org/10.1121/10.0017102

TABLE II. Computational parameters for PE simulations.

Number of Padé coefficients	4
Range grid spacing	50 m
Depth grid spacing	0.5 m
Bottom attenuation coefficient	5 dB/λ
Time window	3 s

instability. Using a high number of internal wave modes in the transport theory model also entails large computation times for the scattering matrix calculations, especially for all the cross-frequency calculations in a broadband setup. The authors compared the transport theory predictions using 50 internal wave modes with calculations involving 900 internal wave modes. The predictions were used to model acoustic mode energies at a single frequency of 75 Hz and cross-frequency coherences of 60–90 Hz against 75 Hz. For the acoustic environment considered in this paper, there did not seem to be much difference between the two predictions, thus, only 50 internal wave modes were used to model the sound speed perturbations.

The transport theory calculations were run on the AQUA cluster at the Indian Institute of Technology (IIT) Madras. The cluster consists of 260 nodes with every node containing 20 cores. Each of the cores had a 2.5 GHz dual Intel Xeon Gold 6248 processor and shared a 192 GB memory. The calculations used a total of 91 frequencies, which were configured to run in parallel, with each job correlating one frequency against the rest of the bandwidth. Each job took about 5–10 days. The differences in compute-times were due to the variations in computational load on the cluster at various times. The nodes were not all available simultaneously for this calculation, and, hence, there were wait-times, which extended the total duration for computations by a large amount. The total time taken to compute all the cross-mode cross-frequency correlations for a 1000 km range took about 3 months.

The broadband PE simulations are based on the split-step Padé solution (Collins, 1993; Jensen *et al.*, 1994). The simulations use the same SSP, buoyancy profile, and potential sound speed gradient given in Fig. 1. To fix the grid sizes of the PE simulations, the simulations were benchmarked against a normal mode sum, which used the same environment profiles as in Fig. 1. The PE simulations converged to less than 1 dB of the normal mode sum for the parameters in Table II. Internal wave induced random sound speed perturbations, $\delta c(r,z)$, were then generated using the method of Colosi and Brown (1998), and added to the background SSP. For mode pulses, the simulated pressure fields from the PE were projected onto the mode shapes, $\phi_n(z)$, at

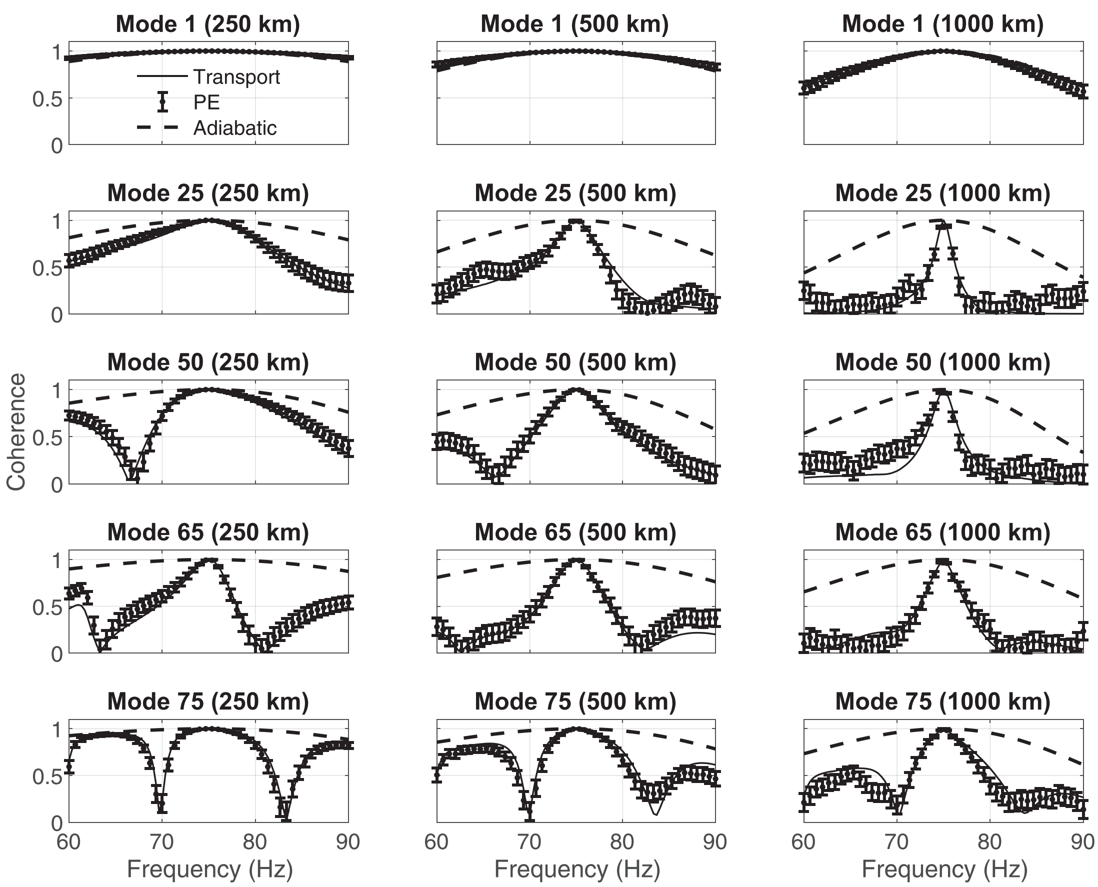

FIG. 2. The cross-frequency coherences of modes from transport theory, PE simulations, and adiabatic approximations at 250, 500, and 1000 km. The standard error bars for coherences of modes at frequency, ω, are calculated using the expression $(1-(\langle\overline{a_n(\omega)a_p^*(\omega_c)}\rangle(r))^2)/\sqrt{n}$, where ω_c is the center frequency of $2\pi\times 75$ Hz (Bendat and Piersol, 2010).

https://doi.org/10.1121/10.0017102

respective frequencies and, from that, the broadband statistics obtained.

III. RESULTS: COMPARISONS BETWEEN TRANSPORT THEORY AND PE SIMULATIONS

This section initially compares the models on a mode-by-mode basis and then proceeds to the time-front.

A. Transport theory predictions vs PE for the individual modes

Figure 2 shows the cross-frequency coherences, $\overline{\langle a_n(\omega)a_n^*(\omega_c)\rangle}(r)$, for a few modes between 1 and 75 and compares them with predictions using separate PE simulations. Comparisons are also included for the adiabatic approximation. The coherences are calculated with reference to a frequency of $\omega_c = 2\pi \times 75$ Hz. The transport theory predictions are close to the averages from PE and mostly within the errorbars. For both methods, mode 1 is highly correlated across frequency at 250 km and 500 km but decorrelates slightly by 1000 km. The coherence bandwidths, however, decrease for an increase in mode number. For modes 65 and 75, at ranges 250, 500, and 1000 km, the coherence is an irregular pattern across frequency and does not steadily decay. The structure of the frequency coherence has some nulls and certain areas where it is high. For some modes, though, such as mode 65 at 250 km and mode 50 at 1000 km, the predictions and PE simulations differ by two errorbars. The adiabatic approximation is a close match to the mode 1 predictions but predicts wider coherence bandwidths for the high modes than the other two methods.

Figure 3 shows mode coherences between frequencies 70 Hz and 80 Hz at 250 km, 500 km, and 1000 km. The two frequencies were chosen so that they were symmetrically located (±5 Hz) at some distance from the center frequency and, yet, not much at the edges of the bandwidth. The results in Fig. 3 can also be extended to other combinations in the source spectrum with similar comparisons. The PE and transport methods show a decrease in coherence across range with the highest coherences across mode number at 250 km and the lowest at 1000 km. Unlike an increase in range, the coherences do not decrease with the mode number. The low modes 1 and 25 are weakly correlated across mode number for all three ranges. Mode 50 at 250 km and 500 km is more correlated than the previous calculation for modes 1 and 25. The mode 50 against the other modes is, however, poorly correlated at 1000 km. A higher mode, such as mode 65, shows even stronger coherence across mode

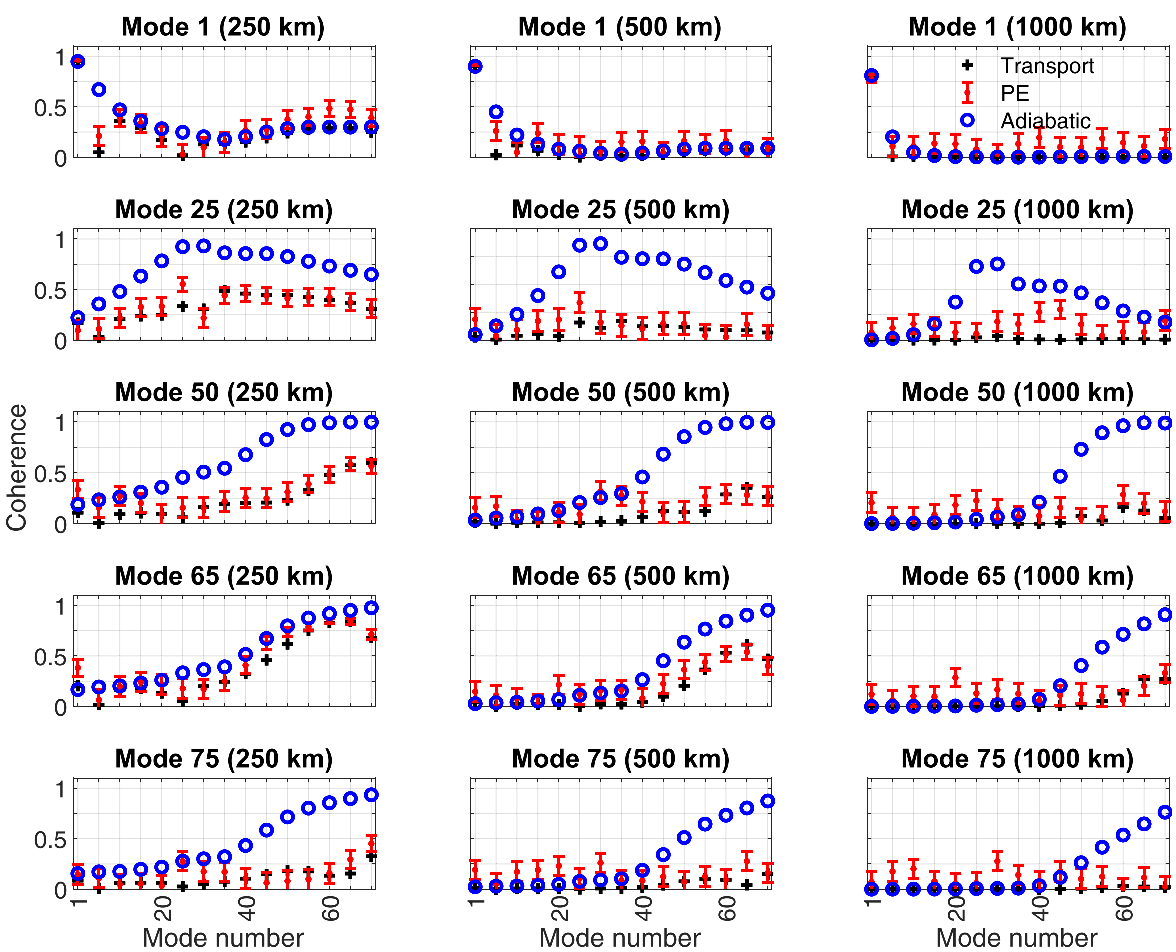

FIG. 3. (Color online) The cross-mode cross-frequency coherences from transport theory, PE simulations, and the adiabatic approximation at 250, 500, and 1000 km. The errorbar calculation is similar to that in Fig. 2.

https://doi.org/10.1121/10.0017102

number for 250 km and 500 km than that for modes 1, 25, and 50. Again, similar to other modes at 1000 km, for mode 65, there is not much correlated across mode number. At 1000 km, there is more decorrelation across all of the mode numbers. The adiabatic mode 1 is poorly correlated with other modes and behaves similar to predictions from the full transport theory. The adiabatic modes 25 and 50 at 250 km are strongly correlated with other modes. The PE and transport methods also predict coherences above zero and, yet, stay a little lower than the adiabatic approximation. On propagating farther than 250 km, the adiabatic approximation for modes 25 and 50 does not compare well with the other two methods. The adiabatic approximation, however, works very well for mode 65 at 250 km and 500 km. The modes are highly correlated across mode number in the approximate case and the full transport theory models. For mode 75, the adiabatic approximation does not work well. The modes are more decorrelated than what the theory predicts. Although Fig. 3 does not show all the correlations, other modes around them also behaved in a similar manner. The low modes, such as modes 1–25, were more decorrelated across mode number, but the coherences improved for the high modes, such as around 55–70, with values close to the adiabatic approximation.

Figure 4 compares the mean intensities of the time series for modes 1, 25, and 50 for the transport theory and PE. There are also comparisons included for the adiabatic approximation and predictions using only the background without any internal waves. All the methods show similar peak values. The adiabatic and the no internal wave case show a similar structure with narrow spreads, which is mostly accounted by the bandwidth. The PE and the transport, however, show larger spreads than the other two due to the effects of scattering. Mode 1 at 250 km does not differ much between all four methods. At 500 km, though, mode 1 pulse shows scattering at times prior to the main arrival. Mode 1 at 1000 km is further spread than the previous ranges. Similar to the 500 km range, the spread occurs at times preceding the main bulk intensity. Mode 25 at 250 km and 500 km shows an increase in spreads for times that follow the main arrival. At 1000 km, mode 25 spreads further, showing scattering on both sides of the main pulse. For mode 50, much of the spread at 250 km and 500 km seems to be from dispersion, and not much scattering is immediately obvious. At 1000 km, however, mode 50 shows an increase in spread in the order of about 0.3 s. The statistics for the other mode pulses lie in between the behavior for the modes in Fig. 4. The scattering on either side of the main arrival is due to coupling-induced contribution from the

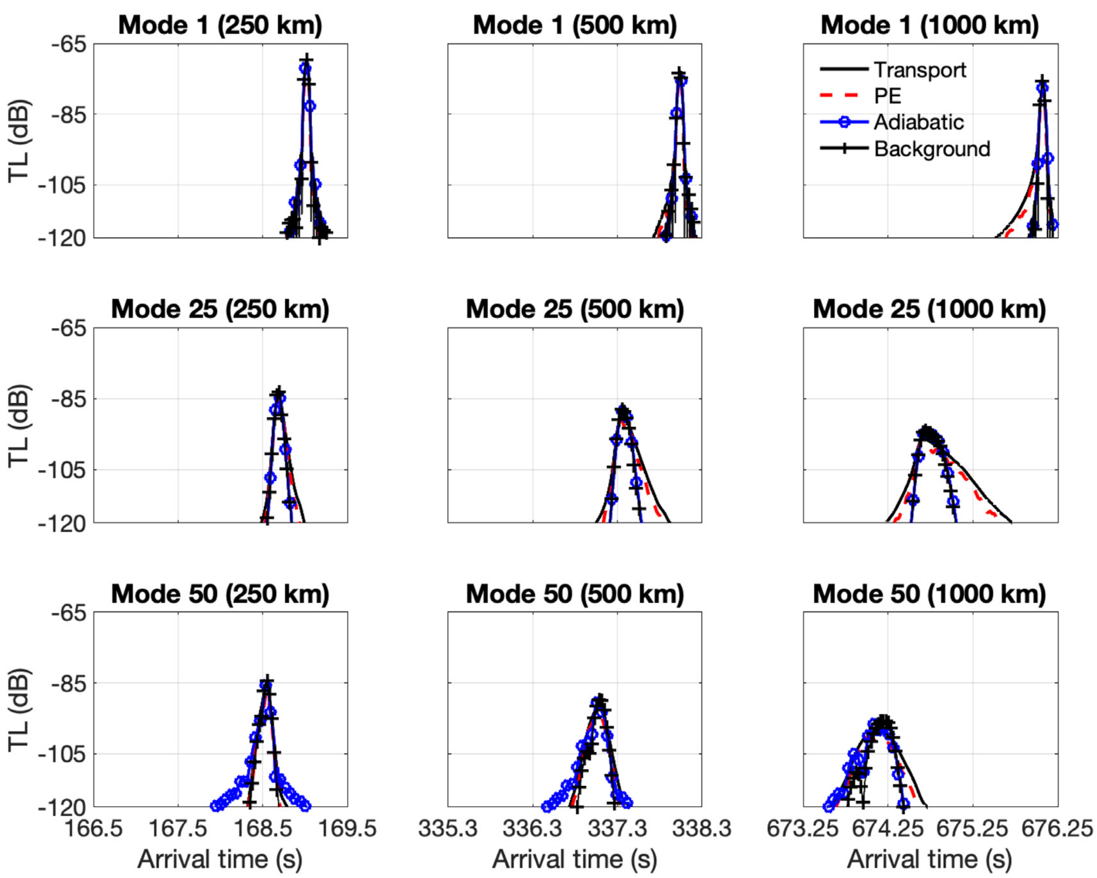

FIG. 4. (Color online) Comparisons between the mean intensity of the mode pulse, $\langle|\beta_n(r,t)|^2\rangle$, predictions from transport theory, and PE simulations (standard error ≈0.37–0.45 dB) for ranges 250, 500, and 1000 km. Predictions using only the background profile and the adiabatic approximation are also included.

respective mode numbers. Mode 1 seems to contain coupling-induced arrivals from modes that arrive early and, hence, the additional spreads toward the times that precede the main arrival. Similarly, mode 25 contains coupling from modes that arrive later than the main arrival. Colosi and Flatte (1996) also made similar observations in relating the trailing and leading edges to the cross-modal scattering contributions.

Figure 5 estimated the temporal spreads from mode pulses, such as the one in Fig. 4, using a 10 dB cut off from the peak for the transport theory predictions and PE averages. The spread from the predictions is within the errorbars of the PE averages. Comparisons are also included for the predictions from the adiabatic model [Eqs. (11) and (14)]. The predictions for the spreads using the full transport theory follow the adiabatic model up to 100–150 km and then show a faster increase beyond 200 km. The transport theory predictions for the lowest set of modes increase the fastest and the highest set of modes the slowest among the three groups. The reason for the fastest increase in time spreads is due to the low values for the cross-mode cross-frequency for these lowest modes (Fig. 3). The adiabatic model for temporal spreads is adequate for ranges up to 100–200 km but fails at greater ranges.

Figure 6 shows the bias of the average mode pulse for both the transport theory predictions and PE simulations. The bias is defined here as the difference of the arrival time estimated from the centroid of the background pulse against the average from PE of transport theory. The estimates for the travel time use the centroid calculated for arrivals within a 10 dB of the peak of the mode time series. Colosi and Flatte (1996) and Flatté and Vera (2003) also estimated the travel time biases for the modes and the time-front, respectively. Transport theory does not yield the average of travel times, but only the average intensity. Figure 6, thus, uses the travel time of the mean intensity to present the bias. At 200 km, transport theory predictions predict a bias similar to that of the average from PE. The transport theory and the PE biases differed by only a few ms. For the resolution afforded by Fig. 6, the two methods at 200 km are on top of each other. At ranges 400 km and 600 km, the predictions are, again, much closer to the estimate from the PE method. For 800 km, the two methods diverge a little and differ by around 25–30 ms at 1000 km. Both the transport theory method and PE predictions, however, show a curious pattern to the biases. The high modes seem to cluster in groups, containing a spread of biases centered around zero. The biases within each group increase linearly, ranging from a

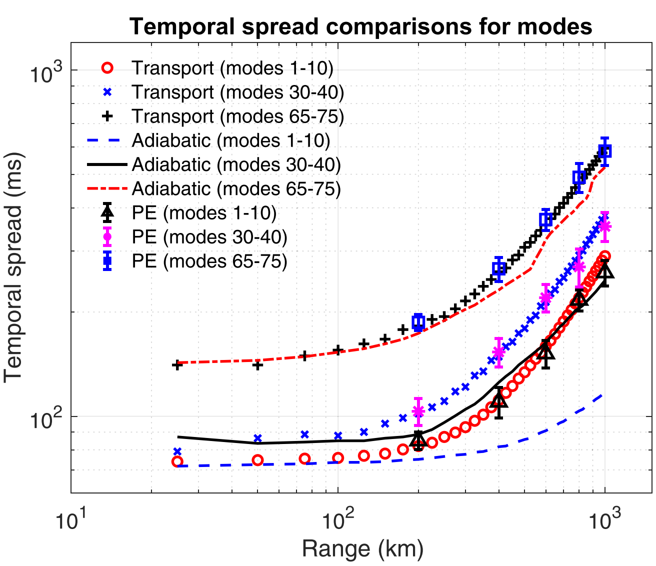

FIG. 5. (Color online) The time spread estimated from transport theory compared against averages from PE simulations. The spread estimated from the mode pulse using adiabatic expression for the mode pulse is also plotted.

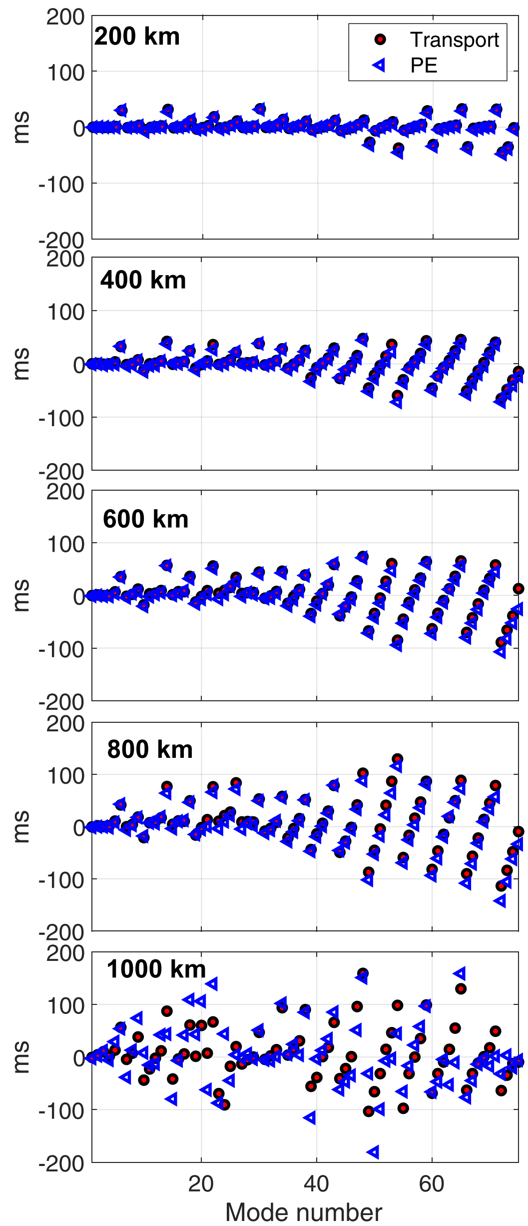

FIG. 6. (Color online) Bias at different ranges for the travel time estimated from the average mode pulse. The transport theory mean intensities were calculated using Eq. (14). For the mean PE mode pulse, the mode pulses for each realization were initially estimated by projecting the pressure time series onto the mode pulses at the respective frequencies and then averaged.

set of negative to positive values. This linear pattern repeats itself across range with the mode-groups having a similar slope.

B. Transport theory predictions vs PE for the time-front

This section will use only the PE and transport theory and also compares the scattering predictions against calculations using only the background profile without any internal waves to appreciate the effects of internal wave scattering. Figures 7–9 show that for ranges 250 km, 500 km, and 1000 km, the transport theory and averages from the PE look quite similar. The scattered time-fronts show smearing of intensities across time and depth. While the background calculations show the interference pattern of the modes with well-defined nulls in depth, they are smeared out in the averages of the two other methods. For example, at 500 km range, in the top row, showing the background predictions around the finale (800–1300 m and 337.9–338.1 s), the low modes are separated in time. Modes 1 and 2 arrive last, preceded by what seem likes modes 5 and higher. The model predictions (verified by PE) show no such distinct modes for the finale, which overlap in time. The 1000 km comparisons in the top row of Fig. 9 also show a similar behavior.

Figure 7 also shows slices of the time-front at 250 km for three different depths. The bottom row shows the time-front at depths 800 m, 1760 m, and 2400 m. The comparisons at 800 m do not show much difference among the three methods. At 1760 m, the biggest difference is for the finale around 168.95 s. The predictions from the background do not show any arrivals toward the end, whereas the transport theory shows scattered arrivals of a transmission loss (TL) value −115 dB, which is 10 dB less than the peak at that depth. The PE simulations are a little less than −115 dB but more visible. This scattering of intensities into a shadow zone is only due to the internal waves, which the background predictions did not include. There is a similar comparison at 2400 m for an arrival that is around a cusp of the early part of the time-front at 168.8 s. For the 500 km range, Fig. 8 shows, in the bottom subplot, slices at 800, 1740, and 3200 m depths. At 1740 m, the transport theory and PE show a much different structure than the background predictions. The latest arrival at 337.85 s for the PE and transport shows much higher levels of intensities than the background, again, due to scattering by internal waves. Similarly at 3200 m depth, the early arrival at 337.2 s shows an arrival that is 15 dB less than the peak. For 1000 km range, Fig. 9 shows the time series at depths 800 m, 1050 m, and 2700 m, which all clearly show the effects of scattering. The transport theory predictions and the PE for the 800 m slice show differences in the order of 5–10 dB for many arrivals. The finale for times after 675.65 s shows much smearing of arrivals with no clear resolution of pulses. The slice at 1050 m also

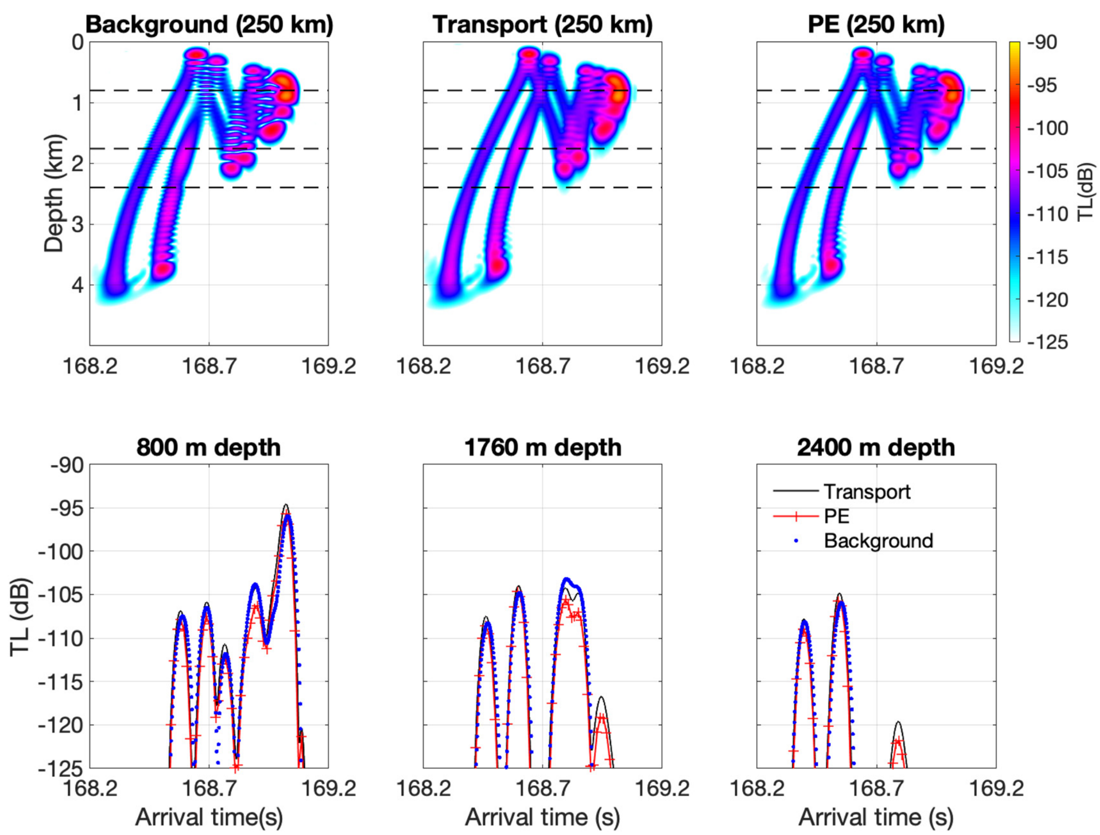

FIG. 7. (Color online) Intensity predictions using only the background SSP (Fig. 1), the mean intensity using transport theory model, and the average of PE simulations (standard error of 0.2–0.5 dB) at 250 km (top row) and the comparisons of intensities for depths 800, 1760, and 2400 (bottom subplots).

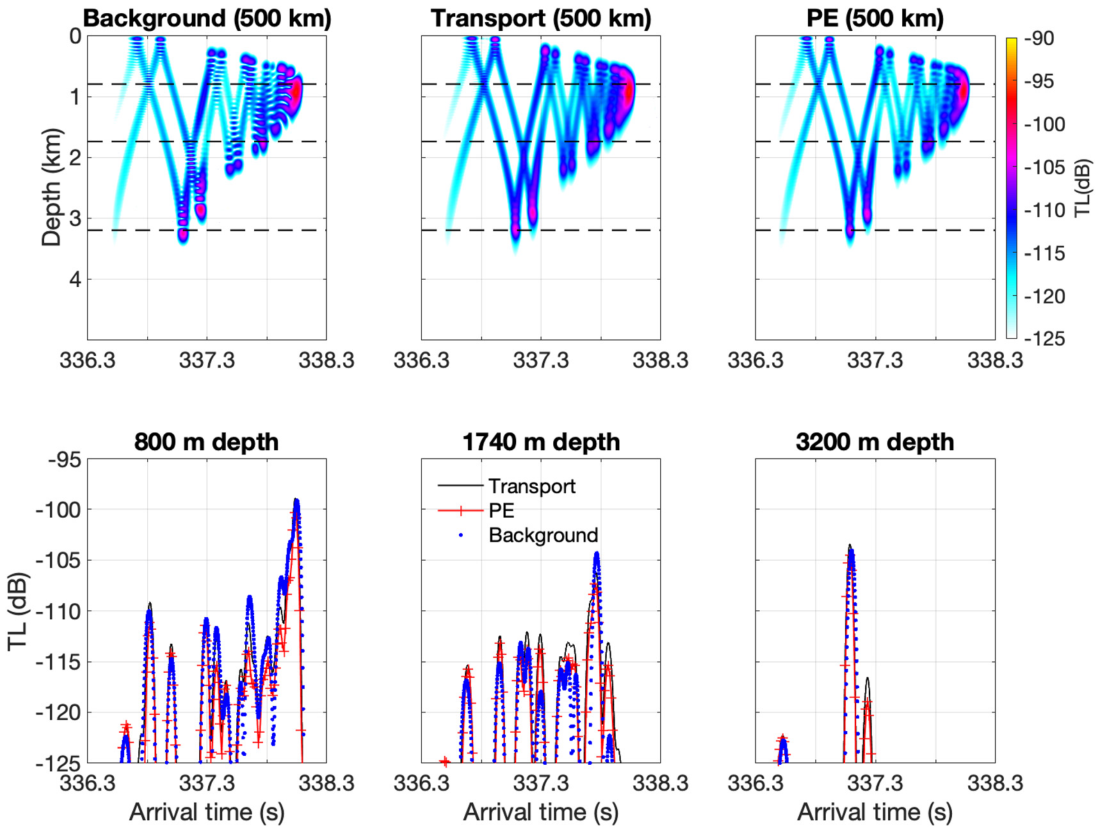

FIG. 8. (Color online) A 2 s window of the time-front for range 500 km with similar comparisons as in Fig. 7. The bottom subplot compares the intensities for depths 800, 1740, and 3200 m.

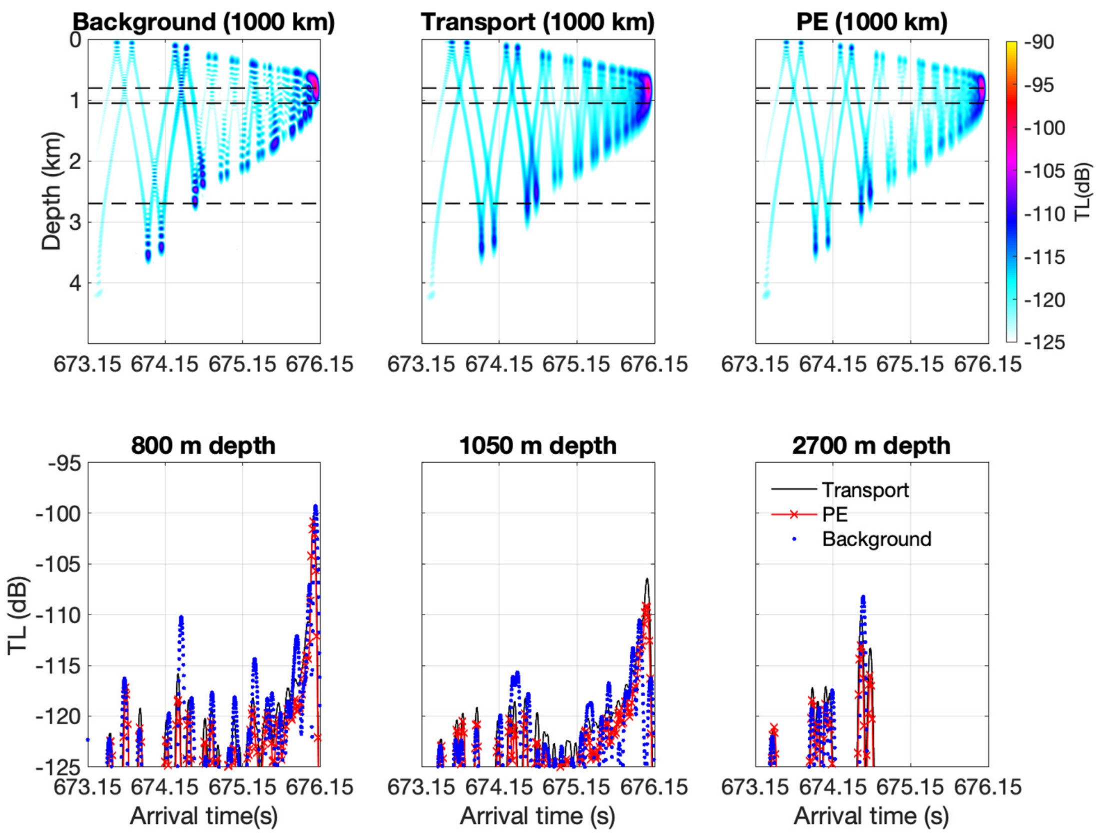

FIG. 9. (Color online) Similar to Fig. 7, a 3 s window of the time-front is shown for range 1000 km. The bottom subplot compares the intensities for depths 800, 1050, and 2700 m.

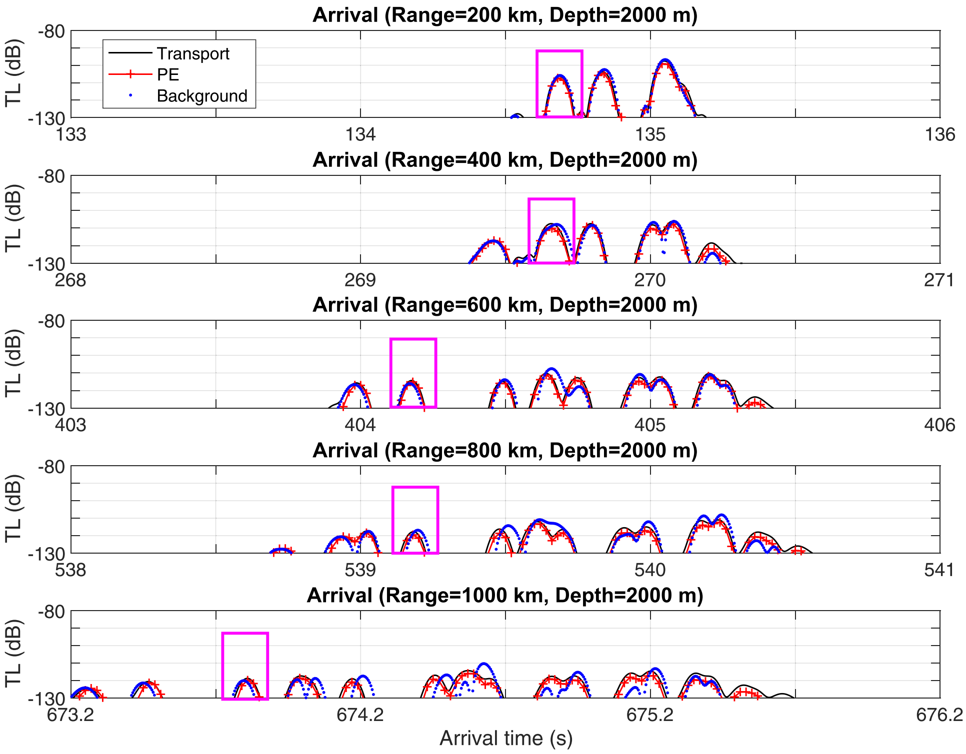

FIG. 10. (Color online) Intensity time series at depth 2000 m for ranges 200, 400, 600, 800, and 1000 km. The arrival indicated within a box is used to estimate the time spread, wander, and bias.

shows similar effects with a peak arrival that seems to be from scattering and exceeds the background predictions by more than 10 dB. The slice at 2700 m depth shows a final arrival that seems to be due to scattering and is only around 5 dB less than the peak.

Moving on to comparisons for other statistics, this section uses slices of the time-front at two separate depths. The two sets of arrivals are chosen to contrast the statistics for the early part of the time-front against the finale. The slices and respective portions at each depth were chosen such that they could be analyzed from transport theory predictions, and also tracked across the complementary PE trials. Figure 10 focuses on statistics for an early part (outlined by a box for clarity) of the time-front by using arrivals at 2000 m

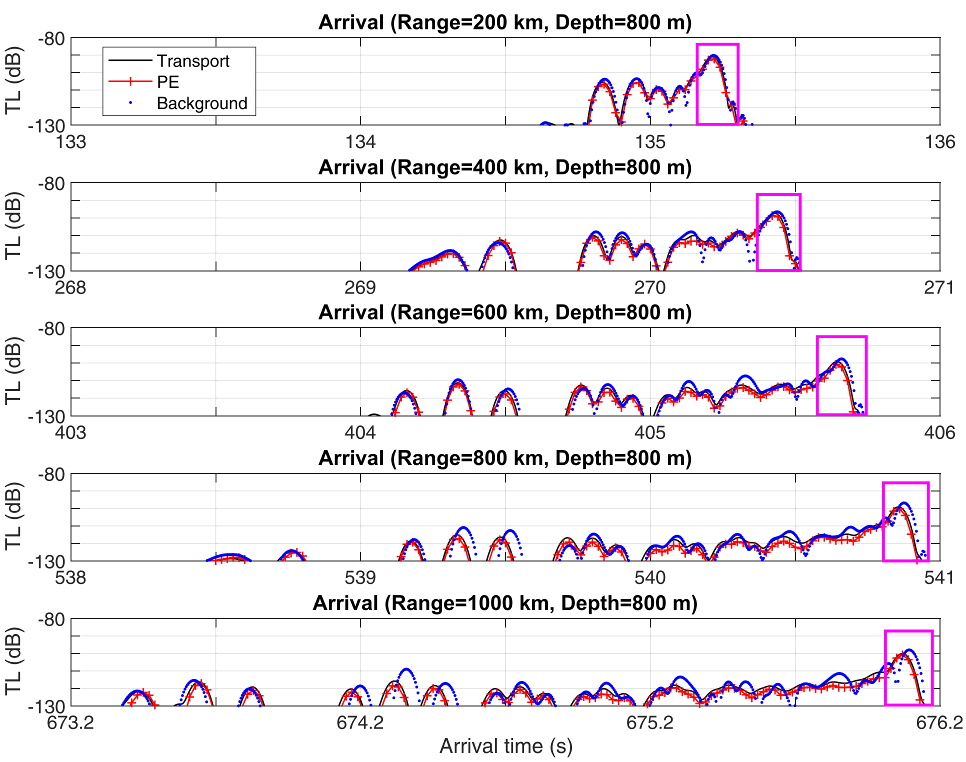

FIG. 11. (Color online) Intensity time series at depth 800 m for ranges 200, 400, 600, 800, and 1000 km. The final arrival indicated within a box is used to estimate the time spread, wander, and bias.

https://doi.org/10.1121/10.0017102

TABLE III. Wander from PE simulations and predictions from the respective modal wander across range for the arrivals in Fig. 10. In brackets, the predictions also show the spread of wanders for the different modes used in the calculation. The standard error of the PE estimate was estimated using the expression $\sigma\sqrt{(1-1/N)-c_4(N)^2}$, where σ is the wander estimated from PE simulations, $c_4(N)=\sqrt{(N-1)/N}(1-1/4N-7/32N^2-19/128N^3)$, and $N=100$ (Cochran, 1934).

Range (km)	Modes	Prediction wander (ms)	PE wander (ms)
200	53–73	2.57 (2.29–2.98)	2.7 ± 0.19
400	22–56	5.5 (4.04–6.67)	4.1 ± 0.28
600	53–75	4.49 (3.87–5.17)	5.2 ± 0.36
800	45–74	5.56 (4.52–7.02)	7.2 ± 0.5
1000	51–75	5.88 (5–6.91)	6.8 ± 0.48

across range. Figure 11 uses the finale at 800 m depth, which is around the axis.

The wanders for the arrivals in Figs. 10 and 11 were predicted using modes and compared with PE. At each range, the mode arrival times for the bandwidth of 60–90 Hz were calculated using the background sound speed profile [Eq. (3)]. The overlap in modal-arrival times against the two different portions marked in Figs. 10 and 11 was used to associate a subset of modes for each of the respective ranges. Table III shows that the arrivals in Fig. 10 are made of modes greater than 20 up to mode 75 at some ranges. On the other hand, Table IV shows that the arrivals in Fig. 11 are mostly made of the low modes, 15 or less. The low modes (Table IV) have a greater wander than the high modes (Table III). This can be explained as follows. The predictions for the wander in Eq. (12) depend on the scattering matrices, I_{nn}, which are a summation across $G_{nn}(j)$, weighted by the respective internal wave strengths, $H(j)$, for each internal wave mode number, j [Eq. (7)]. The $G_{nn}(j)$ depend on the overlap between the internal wave mode shape, j, and the acoustic mode shape, n [Eq. (8)]. The low acoustic mode shapes correlate the most with the low internal wave modes and vice versa for the high. The lowest internal wave modes have the most energy in the spectrum, $H(j)$, and so cause the most wander in the lowest acoustic modes. For comparisons with the model, the wanders were also estimated from the Monte Carlo PE simulations. For each section (Figs. 10 and 11), the arrival times of the peak across PE simulations were first estimated and their sample standard deviation calculated. Tables III and IV show the comparisons between the models based on modes and the PE simulations. The mode-based model and the averages from PE simulations agree.

TABLE IV. Wander from PE simulations and predictions from the respective modal wander across range for the arrivals in Fig. 11. The rest of the caption is the same as that in Table III.

Range (km)	Modes	Prediction wander (ms)	PE wander (ms)
200	1–15	4.76 (4.6–4.84)	4.3 ± 0.3
400	1–12	6.7 (6.5–6.86)	7.2 ± 0.5
600	1–9	8.1 (7.95–8.39)	8.1 ± 0.57
800	1–7	9.2 (9.18–9.59)	9.2 ± 0.65
1000	1–6	10.7 (10.26–10.6)	10.7 ± 0.75

TABLE V. Pulse spread estimates for the early arrivals at 2000 m depth (Fig. 10).

Range (km)	Background (ms)	Prediction (ms)	PE (ms)
200	74	74.7	76.7 ± 5.41
400	74	90.1	93.3 ± 6.58
600	74.7	76.9	76.7 ± 5.41
800	73.2	80.6	80 ± 5.65
1000	79.1	84.2	80 ± 5.64

Tables V and VI show the pulse spread comparisons for the arrivals in Figs. 10 and 11, respectively. The spreads were estimated by calculating the total widths of all arrivals that are within 10 dB of the peak inside the observation window. For the early arrivals, Table V shows that the predictions agree with the averages from the PE. The time spreads for the PE and transport methods, which include the scattering, are both greater than the predictions from background by amount of 5–15 ms. The difference in time spread between the scattering predictions and the background seem to be around the wanders predicted in Table III. For the arrivals in the finale, Table VI shows different amounts of spread for the background at the different ranges. The difference in spread is due to the respective number of (low) modes and the nature of the intra-modal dispersion. The time spreads for the scattering predictions are larger than their counterparts for the early arrival (Table V). In comparison to the mean arrivals in Fig. 10, the finale (Fig. 11) looks more spread, which the time-spread estimates also indicate. The agreement between the PE and the transport theory is within 1–1.5 errorbars for all ranges except 800 km. However, the arrivals around the axis for long ranges, such as 800 km, seem complicated (Fig. 11) with multiple peaks. The discrepancy in the time-spread estimates is potentially because of the nature of the arrival.

Tables VII and VIII compare the bias estimates for the mean time-front from the PE and transport theory. Similar to the mode pulses, the biases measure the difference between the average travel times from the predictions against a similar calculation for the background. The travel times are estimated using the centroid of arrivals within a 10 dB cutoff from the maximum. The biases for the early arrivals in Table VII are smaller than the biases for the individual modes in Fig. 6. The high modes showed a bias of around 100 ms for the high modes at 1000 km (Fig. 6). In

TABLE VI. Pulse spread estimates for the finale at 800 m depth (Fig. 11).

Range (km)	Background (ms)	Prediction (ms)	PE (ms)
200	75.4	95.2	93.3 ± 6.58
400	95.2	106.9	106.7 ± 7.53
600	105.5	116.5	106.7 ± 7.53
800	69.6	112.8	95 ± 6.35
1000	68.8	94.5	86.7 ± 6.12

TABLE VII. Pulse bias estimates for the early arrival at 2000 m depth (Fig. 10).

Range (km)	Prediction (ms)	PE (ms)
200	−2.97	−2.69 ± 0.19
400	−11.19	−10.68 ± 0.75
600	6.13	7.79 ± 0.55
800	−15.23	−14.53 ± 1.02
1000	13.08	16.45 ± 1.16

contrast to the modes, the early arrival in the time-front only showed a bias of 13 ms at 1000 km (Table VII). Similarly, the biases for the finale are also a little less than the individual low modes. While the modes 1–15 at 1000 km show a bias of around ±50 ms, the finale at 1000 km suggests a bias about -26 ms. The bias estimates for the finale are all negative across range, implying the finale, which is made of the lowest modes, consistently arrives earlier than the background.

IV. DISCUSSION

The results in this paper prove that the mode-based transport theory accurately predicts the intensities in all parts of a deep water time-front (Figs. 7–9). The mode-based approach and PE method are based on completely different computational methods and, yet, show almost the same results. The transport theory method seems accurate and also incorporates all of the physics of the waveguide modes and can, hence, be used as a benchmarking tool to predict time-fronts in a random medium. Section II mentioned the time taken to implement such calculations by using the local resources. The lengthy computational times are a potential hindrance for running mode calculations at higher frequencies and longer ranges than discussed in this paper. However, this situation will improve with fast computational resources to establish the mode method as the standard in wave propagation through random media models.

The transport theory method also gives insight into some of the physics of deep water time-fronts. In comparison to the pulse arrivals in the time-front, the mode-view gives a more detailed picture into some of the scattering. Figure 3 showed that the lowest modes are uncorrelated across frequency and mode number. The finale at ranges such as 250 and 500 km are, thus, effectively a sum of uncorrelated mode pulses. This explains the smearing of intensities in the finale of the time-front (Figs. 8 and 9). Although the high modes (such as mode 65 in Fig. 3 and others around it) undergo scattering, they are highly correlated. The high modes roughly share similar turning depths and, hence, their scattering is correlated (Colosi, 2016). This explains why the early parts of the time-front keep their time-depth structure intact. Virovlyansky (1999) offered a ray-based explanation for this phenomenon. Regarding the shadow zones, the modal approach in this paper predicts the amount of ensonification. The high modes scatter toward the low modes and, thus, spread toward later parts of the time-front (example modes 25 and 50 in Fig. 4). While spreading in time, the high modes also scatter energy into deeper depths. This is because the high modes have a larger spread in depth than the low modes. Therefore, this additional spread ends up filling up the shadow zones. Transport theory also seems to provide a mode-based explanation for the ensonification of shadow zones.

For the different sections of the time-front, comparisons in Tables III and IV showed that using an appropriate choice of mode numbers, the RMS wander can be successfully predicted. The mode-based method and path integral method suggest a $\sqrt{R}$ range dependence for the time wander. The similarity lies in both the methods using an adiabatic phase approximation. The difference to be noted, however, is that while the ray method relies on picking the right launch angle and the turning depths, the other method relies on choosing the correct set of modes based on the respective group velocities. Transport theory, though, does not yield analytical predictions that relate the GM parameters to statistics such as spread and bias. The path integral method provides the predictions via expressions for the frequency coherence (Flatte, 1983). The adiabatic model for modes promises such analytical expressions (Colosi *et al.*, 2013). Nonetheless, this paper showed the limitations of the adiabatic theory for predicting the spreads, specifically with regard to high modes and ranges greater than 200 km (Fig. 5). The transport theory method can only give average intensities to estimate the pulse spreads and its predictions are still valuable, especially for estimates around the finale, where the path integral method has issues (Andrew *et al.*, 2016). For the bias predictions, the transport theory method predicts large values for the individual mode arrivals (Fig. 6) and, yet, a relatively small bias for the time-front (Sec. III B). This reduction can be explained as follows. The time-front is a coherent combination of mode pulses with different biases, which add or cancel each other, to yield a net bias that is lower than the individual values.

TABLE VIII. Pulse bias estimates for the finale at 800 m depth (Fig. 11).

Range (km)	Prediction (ms)	PE (ms)
200	−7.94	−7.9 ± 0.55
400	−9.90	−10.37 ± 0.73
600	−16.21	−13 ± 0.91
800	−24.01	−21.73 ± 1.53
1000	−26.69	−26.66 ± 1.88

ACKNOWLEDGMENTS

This research was supported by Naval Research Board India and the Ministry of Human Resources and Development India. The computational results reported in this work were performed on the AQUA Cluster at the High Performance Computing Environment of IIT Madras.

Andrew, R. K., Ganse, A., White, A. W., Mercer, J. A., Dzieciuch, M. A., Worcester, P. F., and Colosi, J. A. (**2016**). "Low-frequency pulse propagation over 510 km in the Philippine Sea: A comparison of observed and theoretical pulse spreading," J. Acoust. Soc. Am. **140**(1), 216–228.

Bendat, J. S., and Piersol, A. G. (**2010**). *Random Data: Analysis and Measurement Procedures* (Wiley, New York), Chap. 8, pp. 249–288.

Chandrayadula, T. K., Colosi, J. A., Worcester, P. F., Dzieciuch, M. A., Mercer, J. A., Andrew, R. K., and Howe, B. M. (**2013a**). "Observations and transport theory analysis of low frequency, acoustic mode propagation in the Eastern North Pacific Ocean," J. Acoust. Soc. Am. **134**(4), 3144–3160.

Chandrayadula, T. K., Periyasamy, S., Colosi, J. A., Worcester, P. F., Dzieciuch, M. A., Mercer, J. A., and Andrew, R. K. (**2020**). "Observations of low-frequency, long-range acoustic propagation in the Philippine Sea and comparisons with mode transport theory," J. Acoust. Soc. Am. **147**(2), 877–897.

Chandrayadula, T. K., Wage, K. E., Worcester, P. F., Dzieciuch, M. A., Mercer, J. A., Andrew, R. K., and Howe, B. M. (**2013b**). "Reduced rank models for travel time estimation of low order mode pulses," J. Acoust. Soc. Am. **134**(4), 3332–3346.

Cochran, W. G. (**1934**). "The distribution of quadratic forms in a normal system, with applications to the analysis of covariance," Math. Proc. Cambridge Philos. Soc. **30**(2), 178–191.

Collins, M. D. (**1993**). "A split-step pade solution for the parabolic equation method," J. Acoust. Soc. Am. **93**(4), 1736–1742.

Colosi, J. A. (**2015**). "A reformulation of the $\lambda - \phi$ diagram for the prediction of ocean acoustic fluctuation regimes," J. Acoust. Soc. Am. **137**(5), 2485–2494.

Colosi, J. A. (**2016**). *Sound Transmission through the Stochastic Ocean* (Cambridge University Press, Cambridge, UK), Chap. 8, pp. 383–387.

Colosi, J. A., and Brown, M. G. (**1998**). "Efficient numerical simulation of stochastic internal-wave-induced sound-speed perturbation fields," J. Acoust. Soc. Am. **103**(4), 2232–2235.

Colosi, J. A., Chandrayadula, T. K., Voronovich, A. G., and Ostashev, V. E. (**2013**). "Coupled mode theory for sound transmission through an ocean with random sound speed perturbations: Coherence in deep water environments," J. Acoust. Soc. Am. **134**(4), 3119–3133.

Colosi, J. A., Cornuelle, B. D., Dzieciuch, M. A., Worcester, P. F., and Chandrayadula, T. K. (**2019**). "Observations of phase and intensity fluctuations for low-frequency, long-range transmissions in the Philippine Sea and comparisons to path-integral theory," J. Acoust. Soc. Am. **146**(1), 567–585.

Colosi, J. A., and Flatte, S. M. (**1996**). "Mode coupling by internal waves for multimegameter acoustic propagation in the ocean," J. Acoust. Soc. Am. **100**(6), 3607– 3620.

Colosi, J. A., Flatte, S. M., and Bracher, C. (**1994**). "Internal-wave effects on 1000-km oceanic acoustic pulse-propagation—Simulation and comparison with experiment," J. Acoust. Soc. Am. **96**(1), 452–468.

Colosi, J. A., and Morozov, A. K. (**2009**). "Statistics of normal mode amplitudes in an ocean with random sound-speed perturbations: Cross-mode coherence and mean intensity," J. Acoust. Soc. Am. **126**(3), 1026–1035.

Colosi, J. A., Scheer, E. K., Flatte, S. M., Cornuelle, B. D., Dzieciuch, M. A., Munk, W. H., Worcester, P. F., Howe, B. M., Mercer, J. A., Spindel, R. C., Metzger, K., Birdsall, T. G., and Baggeroer, A. B. (**1999**). "Comparisons of measured and predicted acoustic fluctuations for a 3250-km propagation experiment in the eastern North Pacific Ocean," J. Acoust. Soc. Am. **105**(6), 3202–3218.

Colosi, J. A., and the ATOC Group (**1999**). "A review of recent results on ocean acoustic wave propagation in random media: Basin scales," IEEE J. Ocean. Eng. **24**(2), 138–155.

Creamer, D. B. (**1996**). "Scintillating shallow-water waveguides," J. Acoust. Soc. Am. **99**, 2825–2839.

Dozier, L. B., and Tappert, F. D. (**1978a**). "Statistics of normal mode amplitudes in a random ocean. 1. Theory," J. Acoust. Soc. Am. **63**(2), 353–365.

Dozier, L. B., and Tappert, F. D. (**1978b**). "Statistics of normal mode amplitudes in a random ocean. 2. Computations," J. Acoust. Soc. Am. **64**(2), 533–547.

Dushaw, B. D., Howe, B. M., Mercer, J. A., and Spindel, R. C. (**1999**). "Multimegameter-range acoustic data obtained by bottom-mounted hydrophone arrays for measurement of ocean temperature," IEEE J. Ocean. Eng. **24**(2), 202–214.

Flatte, S. M. (**1983**). "Wave propagation through random-media: Contributions from ocean acoustics," Proc. IEEE **71**(11), 1267–1294.

Flatté, S. M., and Vera, M. D. (**2003**). "Comparison between ocean-acoustic fluctuations in parabolic-equation simulations and estimates from integral approximations," J. Acoust. Soc. Am. **114**(2), 697–706.

Garrett, C., and Munk, W. H. (**1972**). "Space-time scales of internal waves," J. Geophys. Res. **3**, 225–264, https://doi.org/10.1080/03091927208236082.

Garrett, C., and Munk, W. H. (**1975**). "Space-time scales of internal waves: A progress report," J. Geophys. Res. **80**, 291–297, https://doi.org/10.1029/JC080i003p00291.

Jensen, F. B., Kuperman, W. A., Porter, M. B., and Schmidt, H. (**1994**). *Computational Ocean Acoustics* (AIP, Melville, NY), Chap. 8, pp. 451–488.

Mercer, J. A., Colosi, J. A., Howe, B. M., Dzieciuch, M. A., Stephen, R., and Worcester, P. F. (**2009**). "LOAPEX: The Long-Range Ocean Acoustic Propagation EXperiment," IEEE J. Ocean. Eng. **34**(1), 1–11.

Munk, W. H., Worcester, P. F., and Wunsch, C. (**1995**). *Ocean Acoustic Tomography* (Cambridge University Press, Cambridge, UK), Chap. 2, pp. 30–114.

Periyasamy, S., Chandrayadula, T. K., and Colosi, J. A. (**2022**). "Broadband scattering models for acoustic time-fronts in deep water," in *OCEANS 2022—Chennai*, pp. 1–7.

Reynolds, S. A., Flatte, S. M., Dashen, R., Buehler, B., and Maciejewski, P. (**1985**). "AFAR measurements of acoustic mutual coherence functions of time and frequency," J. Acoust. Soc. Am. **77**(5), 1723–1731.

Udovydchenkov, I. A., and Brown, M. G. (**2008**). "Modal group time spreads in weakly range-dependent deep ocean environments," J. Acoust. Soc. Am. **123**(1), 41–50.

Udovydchenkov, I. A., Brown, M. G., Duda, T. F., Mercer, J. A., Andrew, R. K., Worcester, P. F., Dzieciuch, M. A., Howe, B. M., and Colosi, J. A. (**2012**). "Modal analysis of the range evolution of broadband wavefields in the North Pacific Ocean: Low mode numbers," J. Acoust. Soc. Am. **131**(6), 4409–4427.

Van Kampen, N. G. (**2007**). *Stochastic Processes in Physics and Chemistry* (Elsevier, New York), Chap. 11, pp. 273–287.

Van Uffelen, L. J., Worcester, P. F., Dzieciuch, M. A., and Rudnick, D. L. (**2009**). "The vertical structure of shadow-zone arrivals at long range in the ocean," J. Acoust. Soc. Am. **125**(6), 3569–3588.

Van Uffelen, L. J., Worcester, P. F., Dzieciuch, M. A., Rudnick, D. L., and Colosi, J. A. (**2010**). "Effects of upper ocean sound-speed structure on deep acoustic shadow-zone arrivals at 500- and 1000-km range," J. Acoust. Soc. Am. **127**(4), 2169–2181.

Virovlyansky, A. L. (**1999**). "Comments on 'Mode coupling by internal waves for multimegameter acoustic propagation in the ocean' [J. Acoust. Soc. Am. **100**, 3607–3620 (1996)]," J. Acoust. Soc. Am. **106**(2), 1174–1176.

Virovlyansky, A. L. (**2015**). "Ray-based description of mode coupling by sound speed fluctuations in the ocean," J. Acoust. Soc. Am. **137**(4), 2137–2147.

Virovlyansky, A. L., and Kazarova, A. Y. (**2016**). "Joint statistical moments of mode amplitudes at different frequencies in a random acoustic waveguide," Waves Random Complex Media **26**(4), 564–580.

Wage, K. E., Baggeror, A. B., and Preisig, J. C. (**2003**). "Modal analysis of broadband acoustic receptions at 3515-km range in the North Pacific using short-time Fourier techniques," J. Acoust. Soc. Am. **113**(2), 801–817.

Wage, K. E., Dzieciuch, M. A., Worcester, P. F., Howe, B. M., and Mercer, J. A. (**2005**). "Mode coherence at megameter ranges in the North Pacific Ocean," J. Acoust. Soc. Am. **117**(3), 1565–1581.

Worcester, P. F., Dzieciuch, M. A., Mercer, J. A., Andrew, R. K., Dushaw, B. D., Baggeroer, A. B., Heaney, K. D., Spain, G. L. D., Colosi, J. A., Stephen, R. A., Kemp, J. N., Howe, B. M., Uffelen, L. J. V., and Wage, K. E. (**2013**). "The North Pacific Acoustic Laboratory deep-water acoustic propagation experiments in the Philippine Sea," J. Acoust. Soc. Am. **134**(4), 3359–3375.